STM JOURNALS

Journal of
Polymer & Composites

https://journals.stmjournals.com/JOPC/

ISSN: 2321-2810 (Online)
ISSN: 2321-8525 (Print)
Volume 12, Special Issue 6, 2024
DOI (Journal): 10.37591/JoPC

Research JoPC

Structural, Electrical and Optical Properties of RGO-Incorporated PVA Nanocomposites for UV Shielding Applications

Reddyvari Venugopal [1,*], CH. Srinivas[2]

Abstract

Polymer matrix-based nanocomposites reinforced with appropriate nanoparticles have the potential to exhibit improved electrical, optical and mechanical properties, as well as improved UV-shielding capabilities. These materials are currently being utilised for various commercial applications, such as window shields and automotive components. We prepared reduced graphene oxide (rGO)-incorporated polyvinyl alcohol (PVA) polymer nanocomposites employing a solution casting method. XRD and SEM results confirmed that the rGO nanosheets were dispersed well in the PVA polymer matrix. The presence of rGO in PVA matrices leads to a decrease in the glass transition temperature (T_g) to 87.9 ° C from 101 ° C for pure PVA, where the melting point increases from 200 to 228 ° C. The 0.9 wt.% rGO-reinforced PVA nanocomposites exhibited an increase in DC conductivity of $1.1x10^{-8}$ S/cm at room temperature. The activation energy for PVA incorporated with 0.9 wt.% rGO was 0.096 eV instead of 0.105 eV for PVA. UV-visible spectroscopy investigations were conducted within the wavelength interval between 190 and 1100 nm, during which the absorption edge, the direct band gap, the indirect bandgap, and the Urbach energy were calculated. The UV-Vis absorbance of the composite films exhibits an upward trend as the concentration of nanofillers increases. This outcome holds potential for the utilisation of films as ultraviolet filters. The nanocomposite of PVA-rGO, comprising 0.9 wt.% of rGO nanofiller, exhibited a reduction in the direct band gap from 6.15 eV to 5.0 eV. Similarly, the indirect bandgap also experienced a decrease from 4.72 eV to 3.86 eV. Furthermore, the Urbach energy displayed an increase from 0.402 eV to 0.460 eV for a concentration of 0.9 wt% rGO. The UV shielding ability (% blocking of UV radiation) of the PVA-rGO nanocomposite films monotonically increased from 45.6% for pure PVA to 83.3% for the 0.9 wt.% rGO-incorporated PVA-rGO nanocomposite films. The findings of this study indicate that the utilisation of PVA-rGO nanocomposite materials has the potential to offer significant benefits in various areas such as UV protection, photo detection, adjustable bandgap devices, optical devices controlled by refractive index, and advanced flexible optoelectronic devices.

Keywords: Solution casting, PVA-rGO nanocomposites, XRD, SEM, thermal studies, DC Conductivity and Optical Properties.

***Author for Correspondence**
Reddyvari Venugopal

[1] Assistant Professor of Physics, Department of Physics, Govt. Degree College, Mahabubabad, Mahabubabad, Telangana, India.
[2] Professor of Physics, Department of Physics, University College of Engineering(A), Osmania University, Hyderabad, Telangana, India.

Received Date: March 19, 2024
Accepted Date: July 20, 2024
Published Date: September 26, 2024

Citation: Reddyvari Venugopa, CH. Srinivas. Structural, Electrical and Optical Properties of RGO-Incorporated PVA Nanocomposites for UV Shielding Applications. Journal of Polymer & Composites. 2024; 12(Special Issue 6): S119–S137

INTRODUCTION

EMI shielding materials play a crucial role in modern technology as they help protect electronic devices from electromagnetic interference (EMI) [1,2]. EMI refers to interference caused by electromagnetic fields generated by various electronic devices, communication systems and power lines. This interference can negatively affect the performance and reliability of electronic devices. To combat this issue, EMI shielding materials are used to create barriers that absorb or reflect electromagnetic waves, preventing them

from interfering with sensitive electronic components [3,4]. These materials are designed to attenuate or block electromagnetic waves across a wide range of frequencies. There is a growing demand for superior quality EMI shielding materials due to the increasing use of electronic devices and the subsequent rise in electromagnetic radiation. Traditional shielding materials, such as copper and aluminium, have been widely used in the past [5,6]. However, with advances in technology and the need for more efficient shielding, unconventional materials have gained prominence. Ceramic, polymeric and carbon matrix composites are examples of unconventional EMI shielding materials that are being explored. These materials offer advantages such as flexibility, corrosion resistance and good electrical conductivity. Carbon nanostructures have gained attention due to their unique properties. However, the synthesis of carbon nanostructures can be complex and expensive, and they may exhibit poor electromagnetic absorption characteristics. In order to overcome these limitations, researchers have investigated the combination of carbon nanostructures with polymers. The addition of carbon nanostructures can enhance the electromagnetic absorption characteristics of the materials, making them more efficient for EMI shielding applications. Several factors influence the efficiency of EMI shielding materials. The dispersion of conductive polymers, electrical conductivity, dielectric characteristics and shape of the composite are all important considerations. Optimising these factors can lead to improved shielding effectiveness and performance [7].

Therefore, the fortification of appropriate nanoparticles in polymer matrix-based nanocomposites can provide enhanced mechanical, electrical and optical properties as well as superior UV-shielding ability. These categories of materials have been artificially produced for a variety of commercial applications, including, but not limited to, the automotive industry and the manufacturing of window shields. Currently, the introduction of nanomaterials has significantly improved the overall performance of polymers due to their increased surface area, smaller nanoscale dimensions, quantum confinement effects and robust interfacial interactions [8]. It is important to note that these materials play a vital role in both industrial and academic contexts [9,10]. In this context, poly(vinyl alcohol) (PVA) has emerged as a synthetic biodegradable polymer possesses a multitude of desirable properties, including non-toxicity, lack of odour, thermal stability, transparency and the ability to exist in a semicrystalline state [11]. The semicrystalline nature of PVA is attributed to the presence of hydrogen bonding between its individual polymer chains [12]. PVA serves as an exemplary polymer for film formation as a result of its water solubility, biocompatibility and favourable physical properties. Additionally, this polymer exhibits chemical stability [13]. In the realm of biomedical applications, PVA composites, including PVA gels, find utility in various domains, such as the production of contact lenses, artificial heart surgery, drug delivery systems and wound dressings [14]. The introduction of an appropriate nanofiller into a polymer, for instance, PVA, can induce interactions with its amorphous or crystalline components, thereby modifying its inherent characteristics. Moreover, PVA demonstrates exceptional optical transparency and serves as a dielectric material, rendering it environmentally friendly and suitable for numerous applications.

Furthermore, reduced graphene oxide (rGO) has a direct bandgap in the range of 1.0-1.69 eV, a strong breakdown field, excellent thermal stability, and favourable environmental characteristics. It is also quite inexpensive. Therefore, it is useful in a wide range of industrial, scientific and medical applications. In this study, the solution casting method was used to create rGO nanosheets incorporated PVA matrix nanocomposites at various weight compositions, such as PVA + x wt.% of rGO, where x = 0, 0.3, 0.6, and 0.9. The most notable amount of nanofiller was 0.9 wt.%. A higher concentration of filler loading results in further nanosheet agglomeration, which disrupts the shape of the composite surface and other attributes [15]. This method offers a practical way to create multifunctional composites that absorb microwaves.

MATERIALS AND METHODS

Fabrication of PVA-RGO Nanocomposites

The preparation of PVA-rGO nanocomposite films was carried out using the solution casting method, which involved the use of AR grade polyvinyl alcohol (PVA) [99%, SD Fine Chem Ltd.] and reduced graphene oxide (rGO) [with a sheet thickness ranging from approximately 0.8 to 2 nm and dimensions

of about 5-10 μm; Ad-nano Technologies] as constituents of polymer matrix-based nanocomposites. A detailed depiction of the procedure employed for fabricating the PVA-rGO nanocomposite films can be observed in Fig. 1. In order to ensure accuracy and precision, the stoichiometric ratios of the precursors were meticulously measured, employing a delicate balance for this purpose. The initial step involved the dissolution of 5g of PVA in 80 ml of double-distilled water, followed by a thorough stir for a duration of 9 hours, resulting in the formation of a homogenous thick gel. Subsequently, a quarter of this gel was transferred to a Petri dish and subjected to the drying process, yielding a pure PVA film. Simultaneously, the remaining three-quarters of the gel was added with 0.3 wt.% rGO nanosheets, which were already dispersed in 20 ml of double distilled water. This mixture was stirred at 600 rpm for a period of 24 hours, ensuring a good dispersion without any agglomeration. To further enhance the homogeneity of the amalgamated PVA gel, it was subjected to ultrasonic treatment, using probe sonication at a power of 360 W for a duration of 15 minutes. Following this step, the gel mixture was poured into a Petri dish and left to dry in a laboratory fume hood (IGene Labserve) under a dust-free environment at ambient temperature, thereby facilitating the production of the desired nanocomposite films. This entire process was repeated for different weight percentages, namely 0.6 wt.% and 0.9 wt.% of rGO, resulting in the formation of a series of PVA-rGO nanocomposite films. Subsequently, these dried films were carefully removed from the Petri dishes, stored in a vacuum desiccator to prevent any kind of contamination, and subsequently used for further characterisation.

Characterisation Techniques

The structural properties of the PVA-rGO nanocomposite thin films were analysed using the SHIMADZU XRD-7000 X-ray diffractometer with Cu(Kα) at a wavelength of 1.5406 Å. In order to investigate surface morphology, the FEI Quanta-250 SEM device, coupled with an energy-dispersive X-ray detector at 10 kV, was used. Thermal analysis of the PVA-rGO nanocomposites was conducted using the SHIMADZU DSC-60 plus thermal analysis machine. DSC studies were conducted with a heating rate of 10 °C/min in the temperature range of 20 °C to 400 °C. To measure DC electrical conductivity, a 4-probe DC electrical conductivity system with a heating chuck was employed. To ensure accurate measurements, a high-conductivity silver coating was carefully applied to establish ohmic contact. Lastly, the absorption data was obtained using the SHIMADZU UV–1800 series UV Vis spectrometer, which operates in the range of 190-1100 nm.

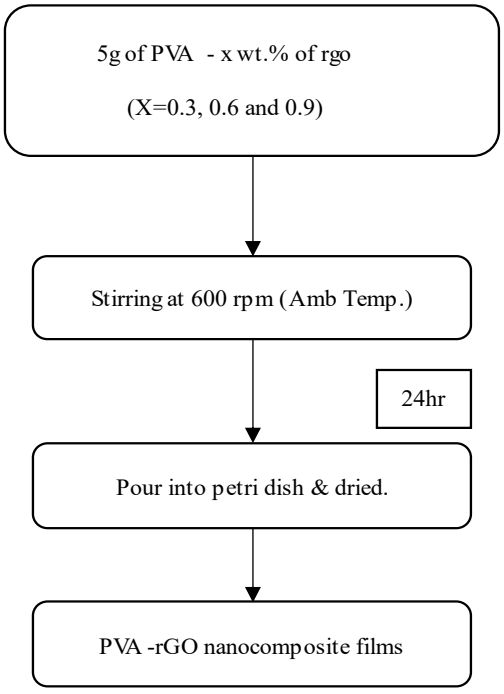

Figure 1. Procedure for the preparation of PVA-RGO nanocomposite films.

Figure 2. Stirring machine for the preparation of PVA-RGO nanocomposite films.& Images of the Prepared PVA-RGO Composite Films.

RESULTS AND DISCUSSIONS

X-Ray Diffraction Analysis

The present study utilised X-rays to study the impact of rGO dispersion on the crystal structure of both pure PVA and PVA-rGO nanocomposite films. The pure PVA diffraction pattern exhibited a singular, prominent and intense peak at 2θ~19.5°, which was accompanied by a corresponding lattice spacing between planes (d) of 0.46 nm. This peak can be ascribed to the (101) planes of semicrystalline PVA. After the introduction of rGO nanosheets into the PVA polymer matrix, the diffraction peaks shifted to 19.58°, 19.51° and 19.51°for the resultant nanocomposite films. The XRD pattern of the composite films shows a small, sharp peak of rGO at 2θ~26.6° [16]. Pure PVA and composite films had significant low intensity peaks at 2θ=41°. The positions of the peaks exhibit a remarkable degree of similarity in all the nanocomposite films that were prepared, indicating a consistent and homogeneous distribution of rGO nanosheets within the PVA matrix [17].

The PVA matrix does not change structurally when rGO nanosheets were added [18]. This phenomenon can be attributed to the considerable amount of hydroxyl (-OH) groups present on the backbone of PVA [19]. The intermolecular interaction of the PVA chains is reduced because of the interference among the rGO and PVA chains. The amorphousness of PVA slightly increases as rGO is added. The diffractograms indicate that the intensity and size of the peak increase proportionally with increasing rGO concentration [18]. In Fig. 3, the XRD peaks in the nanocomposite films become broader with increasing filler content. This could be because the rGO nanosheets modify the amorphous PVA phase [20,21]. The successful preparation of PVA-rGO nanocomposite films is evidenced by the presence of rGO nanosheets, that reinforce an altered amorphous structure in the films.

Scanning Electron Microscopy (SEM) Studies

Surface morphology studies

Figure. 4 depicts the SEM micrographs depicting the PVA-rGO composites and pristine PVA films. These films exhibit a smooth and analogous morphology with variable roughness levels. The surface morphology of PVA is neat and smooth. In its amorphous state, PVA is submicroscopic [22]. In Figure. 4 (b to d), rGO nanosheets were present at 0.3, 0.6 and 0.9 wt% in the PVA polymer matrix.

SEM revealed that the rGO sheets exhibited a uniform distribution throughout the PVA polymer. It offers composites more flexibility and strength than pure PVA [23]. The upper surface of these films had a few small white dots with no visible cracks. The surface morphology revealed that the rGO sheets agglomerated and were incorporated into the nanocomposite films. The rGO sheets tend to agglomerate and emerge as microsheets. Agglomeration increases as the rGO content increases. The rGO nanosheets is homogenous and uniform within the PVA polymer matrix. On observation, it was observed that the physical manifestations of the samples underwent a noticeable transformation from transparent, indicative of pure polyvinyl alcohol, to translucent, reflective of composite materials. These findings indicate that rGO is a suitable nanomaterial for dispersing and diffusing other nanometre sized materials [24].

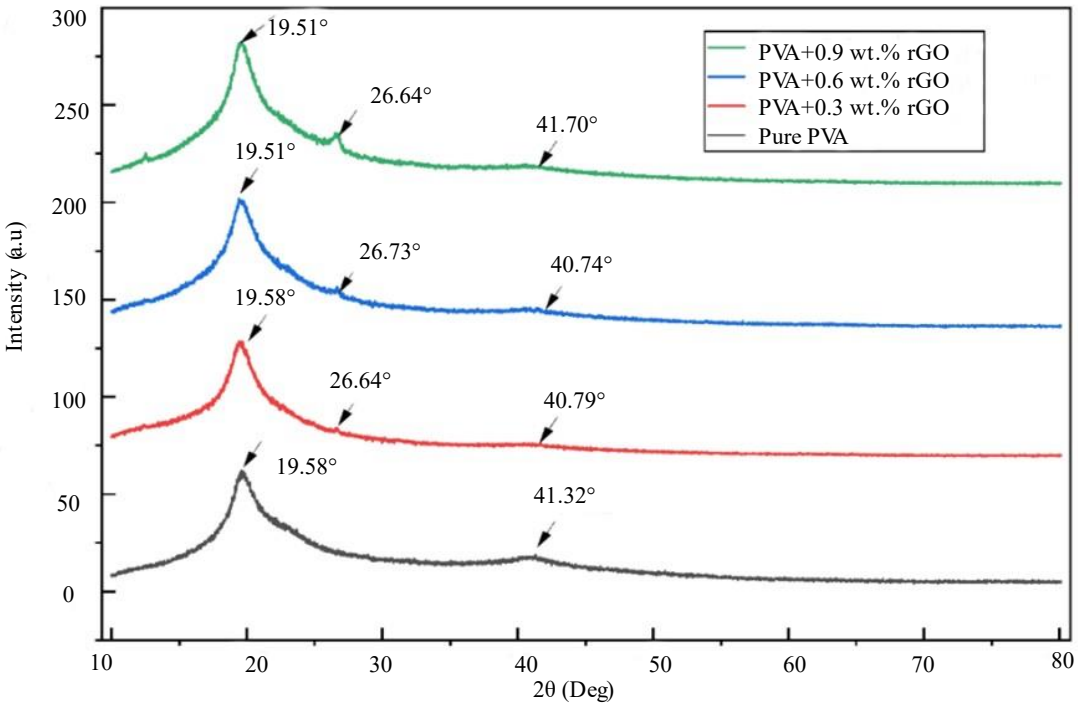

Figure 3. XRD fingerprints of the PVA-RGO nanocomposite films.

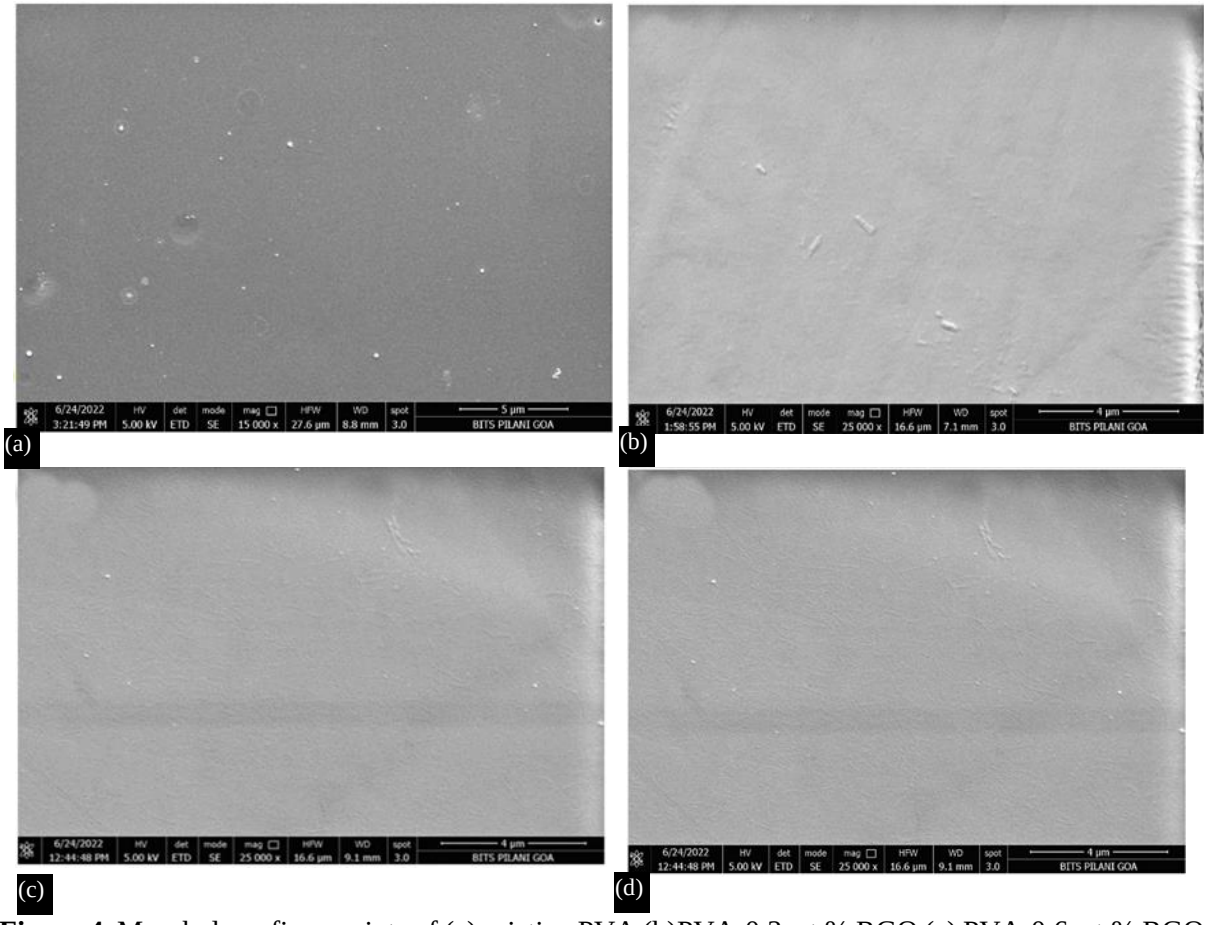

Figure 4. Morphology fingerprints of (a) pristine PVA (b)PVA-0.3 wt.% RGO (c) PVA-0.6 wt.% RGO (d) PVA-0.9 wt.% RGO nanocomposite films.

Differential Scanning Calorimetry (DSC) Studies

The thermal properties of the PVA and PVA-rGO nanocomposite films were examined using DSC analysis and are shown in Fig. 5. The samples were heated at a rate of 10 °C/min. The existence of endothermic peaks in all the curves specifies the glass transition of the samples. Table 1 lists the recorded values of the observed T_g, T_m and T_d. The composites have lower T_g and higher T_m values than those of the pure PVA sample. The T_g values of the PVA-RGO nanocomposites exhibit a small decrease with increasing RGO content [16]. However, it is crucial to note that the increased possibility of nanosheet agglomeration causes a variation in all of the degradation characteristic temperatures for higher rGO wt.% nanocomposites. This is because, during agglomeration, the nanostructure of the RGO nanosheets is converted to a microstructure, causing the thermal stability of the nanocomposites to be altered [17]. Therefore, dispersed nanosheets have fewer impacts in protecting macromolecular chains from heat than dispersed nanosheets at lower concentrations.

Figure. 5 shows a monotonic trend, indicating that the T_g of PVA-rGO nanocomposites shows a notable trend of decreasing with increasing wt% rGO in composite films [18]. The degree of freedom of the polymer chain is affected by many factors. Two primary elements compete with each other in most cases involving nanocomposites. The first element entails the utilisation of a polymer film on the exterior of the nanoscale particles, thereby increasing the number of available states and the randomness of the nanocomposite systems. This phenomenon subsequently leads to a reduction in the T_g value. Second, the incorporation of organic nanomaterials within the polymer matrix leads to a decreased density of the configuration states of macromolecules [16]. This makes it possible for the disorientation entropy to increase, leading to a decrease in T_g. Nevertheless, it is important to note that nanosheet agglomeration, microsheet formation, and film uniformity may vary between samples.

Figure 5 also shows the existence of endothermic peaks at 323-326 °C in all samples, which are clear indications of the decomposition of the PVA-rGO nanocomposite films. Additionally, minor endothermic peaks caused by water vapour were identified at low temperatures near 100 °C [16]. The previous studies mentioned almost identical results for the other nanocomposites characterised by extremely low loadings [19]. The inclusion of only 0.9 wt% rGO nanosheets in PVA increased the melting point to 222.8 ^{0}C from 2000 ^{0}C for pure PVA, as shown in Table 1.

Table 1. Glass transition (T_g), melting point (Tm), and decomposition (Td).Temperatures of the PVA-rGO composite films.

S.no	Sample	Glass transition temperature.T_g (^{o} C)	Melting pointT_m (^{o}C)	Decomposition tempT_d (^{o}C)
1	Pure PVA	101.7	200	323
2	PVA-0.3 wt. % rGO	98.8	208.6	324
3	PVA-0.6 wt. % rGO	93.77	221.6	325.8
3	PVA-0.9 wt. % rGO	87.97	222.8	326.2

DC Electrical Conductivity Studies

Current-voltage (I-V) characteristics

The two-point probe (TPP) method was used to study the I-V characteristics of virgin PVA and PVA-rGO nanocomposite films [25]. The voltage range was ±10 V with a step of 0.5 V. In the present study, we used a narrow voltage range chosen to estimate conductivity [26]. In the voltage range of ±10 V, the PVA and composite films demonstrated non-linear electrical behaviour, as shown in Figure. 6. A common current flow pattern is observed in typical PVA composites, which have substantially lower conductivities. Moreover, the composite films produced a non-linear response when the rGO concentration increased, as shown in Figure. 6. The I-V characteristics of PVA and the composite films indicate that these materials are non-ohmic due to polarons and bipolarons [27]. These characteristics indicate that the composite films exhibit behaviours that are different from those of PVA, but the current level is more significant in the composites than in PVA.

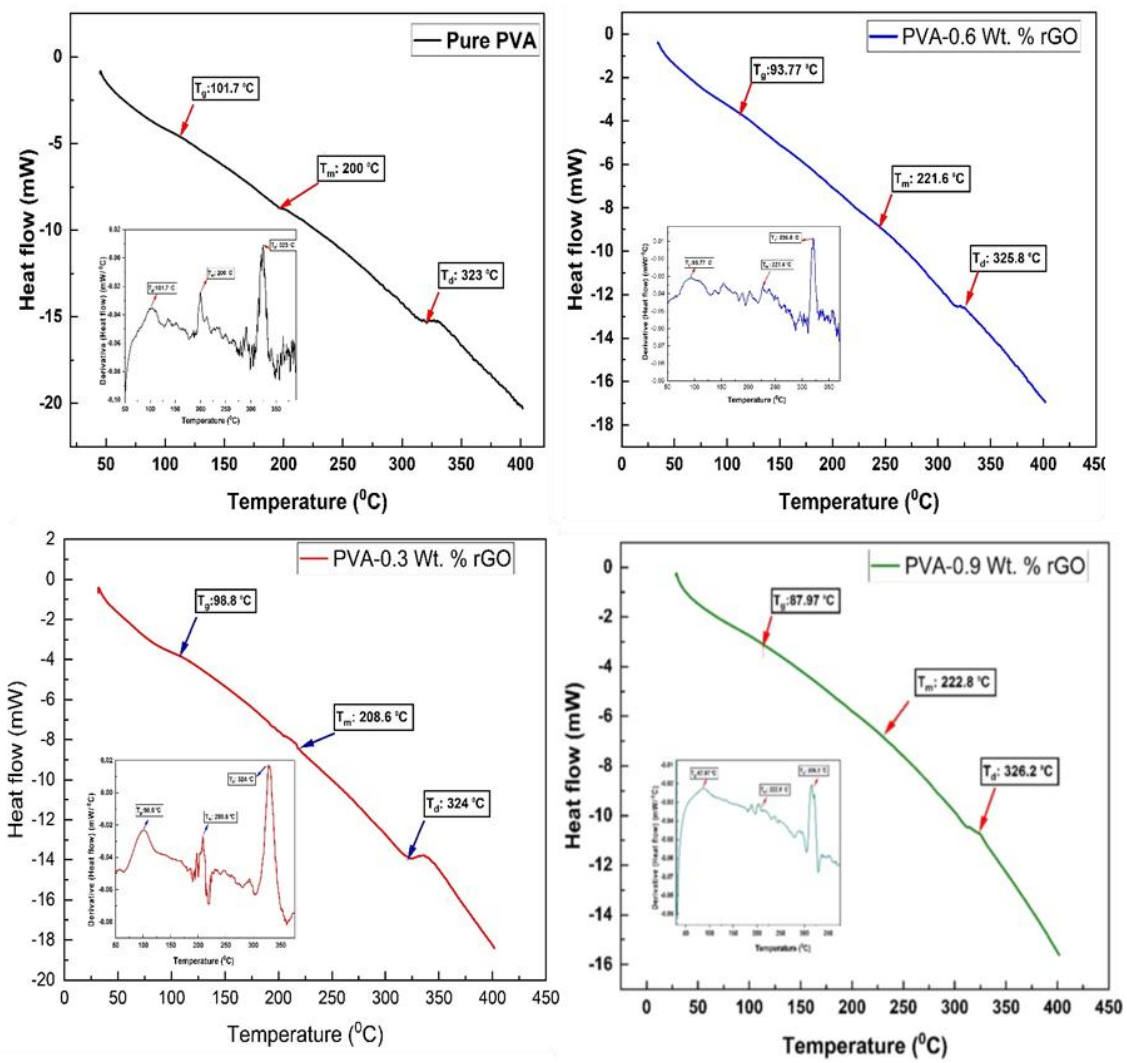

Figure 5. DSC Thermograms of the PVA-rGO nanocomposites.

DC electrical conductivity and activation energy

The DC conductivity of all samples was evaluated by detecting the high resistance of the sample and using the sample dimensions computed from equation 1 [27].

$$\sigma = (t/RA)\ Scm^{-1} \quad (1)$$

The thickness of the film is represented by t (cm), its area is A (cm^2), and the resistance of the film is R (ohm).

Figure. 7 displays the variation in the DC conductivity of the PVA and PVA-rGO nanocomposites with temperature. The DC conductivity increases with the temperature and nanofiller concentration (wt.%). The conductivity increases exponentially in the temperature range of 320-380 K, where in the polarons have enough energy to hop between many localised states. Materials lacking a distinct crystalline structure exhibit a conductivity behaviour that is unique to their composition. The enumerated conductivity values for all samples can be found in Table 2. Determination of the activation energy for each sample was conducted using DC conductivity measurements with variations in sample temperature, for which the experimental data were fitted with Equation 2.

$$\sigma_{(T)} = \sigma_0 \exp(-\Delta E/kT) \quad (2)$$

where σ_0 is a constant, ΔE is the activation energy, k is the Boltzmann constant in eV/k, and T denotes the Kelvin temperature [28].

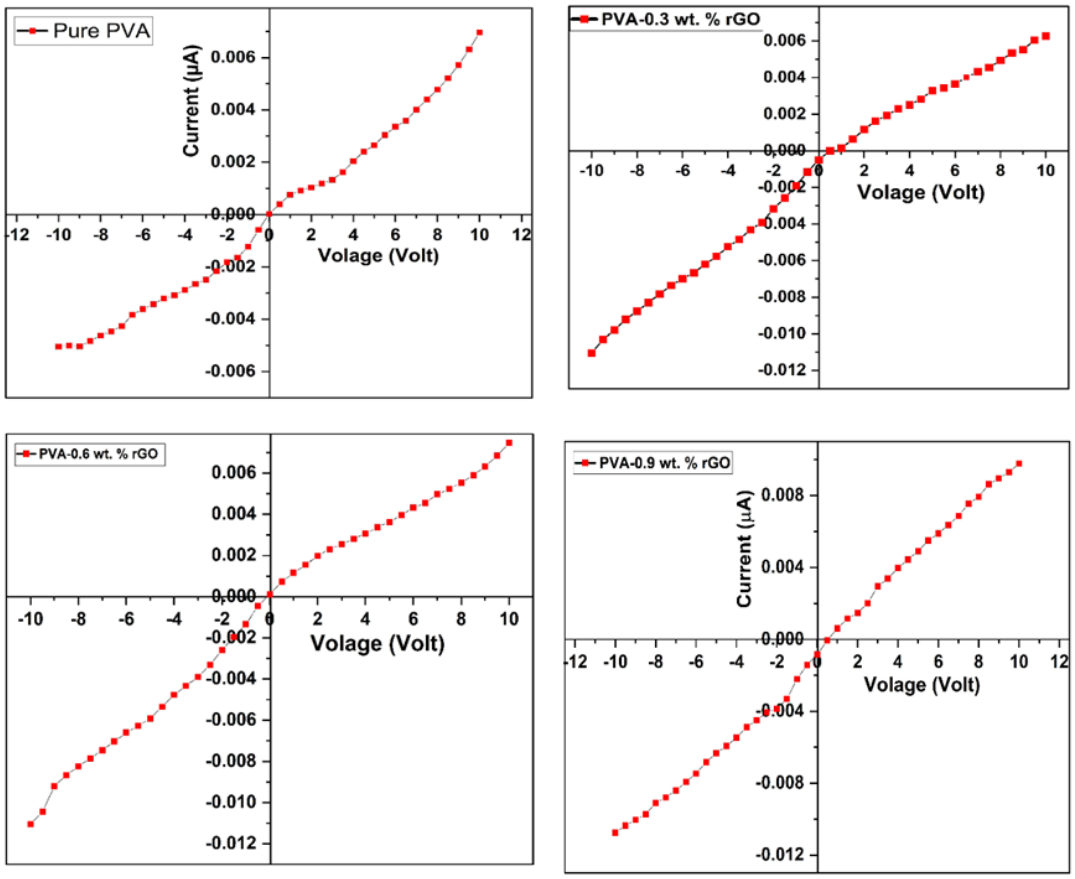

Figure 6. I-V characteristics of the PVA-rGO nanocomposite films.

Using the least-squares approach, we have been able to determine the activation energy by plotting a graph log(σ) *vs*. 1000/T, as depicted in Figure. 8. By analysing the experimental data, a linear regression was performed to determine the activation energy of PVA and the composite film. The results showed that the activation energy is more pronounced at lower temperatures compared to higher temperatures. This suggests that the interaction between rGO and PVA is stronger at lower temperatures. Furthermore, it was observed that the activation energy decreases as the nanofiller content increases. Therefore, it can be concluded that the nanofiller participates in the conduction mechanism above the glass transition temperature. PVA-rGO nanocomposites dominate the charge transport mechanism at lower temperatures than pristine PVA [29].

Table 2. The DC Electrical Conductivity and Activation Energies of PVA-rGO nanocomposites.

Sample	DC Conductivity (S cm ^{1})	Activation energy(eV)
PVA	1.506 x 10^{-12}	0.10459
PVA-0.3 wt.% rGO	4.736x 10^{-11}	0.10458
PVA-0.6 wt.% rGO	2.507 x 10^{-10}	0.0978
PVA-0.9 wt% rGO	1.1018 x 10^{-8}	0.0956

UV-Vis Spectroscopy - Study of Optical Properties

Optical absorption

Figure. 9 shows UV-vis absorption spectra of PVA-rGO nanocomposite films that were fortified with rGO. The pure PVA film absorbed most of the light below 250 nm in the UV range due to its $(CH=CH)_2$-CO skeleton, π-π* transition, and n-π* transition [30,31]. The band gap of PVA is responsible for the sharp decrease in absorption in the 242–266 nm region. Pure PVA films showed low absorption at visible light wavelengths, while nanocomposite films showed strong absorption between visible light and UV light [31].

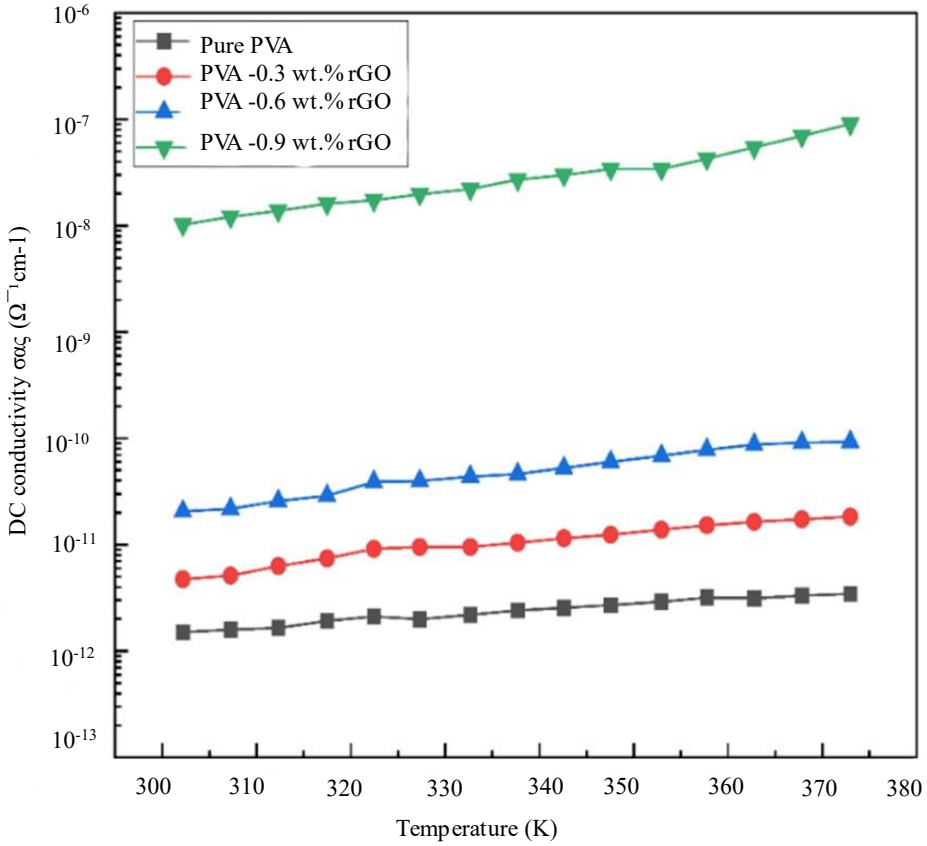

Figure 7. DC electrical conductivity of the PVA-rGO nanocomposite films.

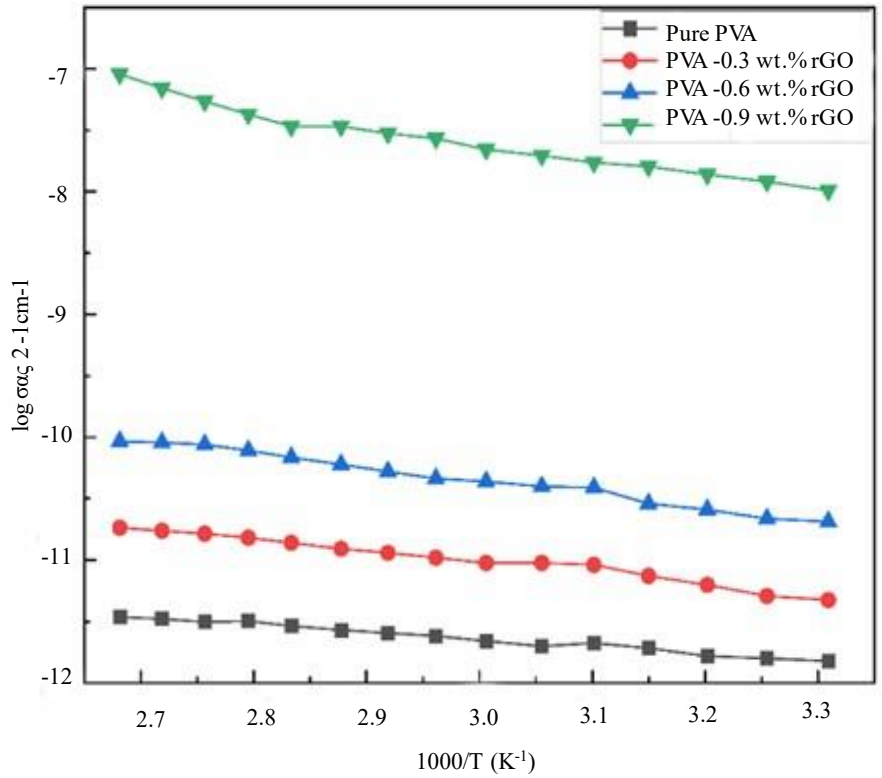

Figure 8. Determination of the activation energy at different temperatures log(σ) vs. 1000/T for PVA-rGO nanocomposites.

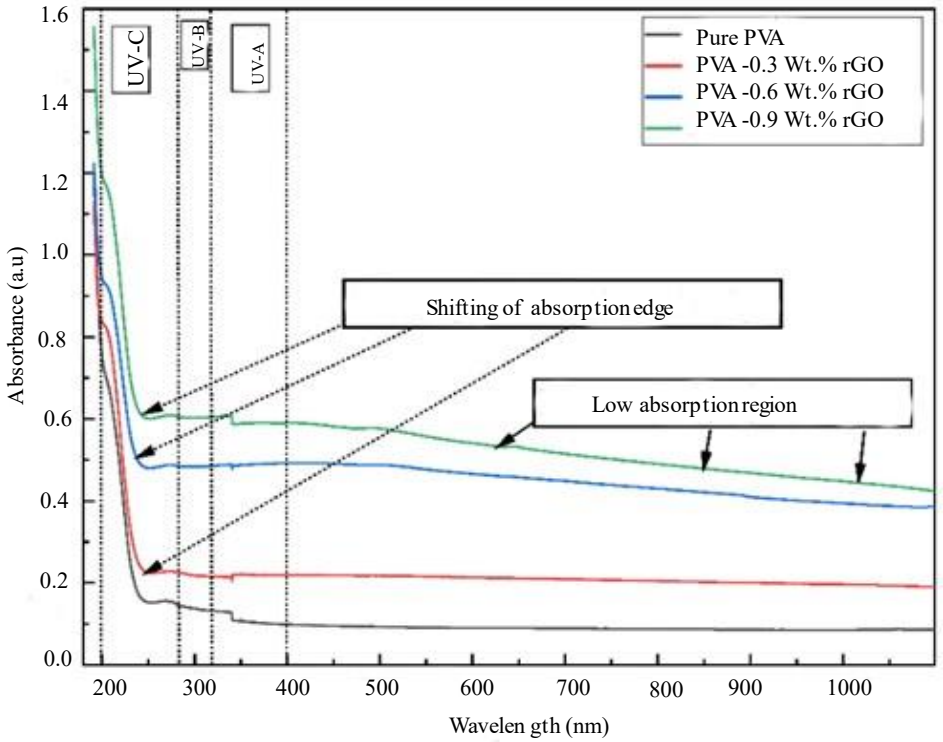

Figure 9. Changes in the absorbance of PVA-rGO nanocomposites with wavelength.

The nanocomposite films have a higher absorption of light at higher wavelengths. The absorption edge of the nanocomposite films increased from 216 nm for pure PVA to 219-226 nm. In addition, a small peak in absorbance at around 330 nm was observed in the nanocomposite film spectra, indicating the presence of C=O bonds in the rGO. The absorption edge of the nanocomposite films shifts to longer wavelengths as the amount of rGO increases. This shift in the absorption edge can be attributed to hydrogen bonding between the hydroxyl functional groups of PVA and rGO. Figure.10 shows that increasing the weight percentage of rGO nanosheets leads to a shift in the optical absorption edge to lower energies. According to related research, absorption enhancement is connected to the charge-transfer transition [33]. The results indicate that nanocomposites can absorb a wide variety of radiation, making them an ideal choice for UV protection. Therefore, these nanocomposite films are highly recommended as good UV filters.

Determination of the absorption edge

The absorption edge is commonly regarded as the optical energy gap that is minimal in each material. Lambert–Beer's law was used to determine the absorption coefficient (α) of composite films with a given thickness (t) and optical absorbance (A) through the application of experimental optical absorption data through equation 3 [34].

$$\alpha=2.303(A/t) \quad (3)$$

Figure. 9 shows the absorbance data for thin films of PVA-x by wt.% rGO, where x represents the weight percentage of rGO (0, 0.3, 0.6, and 0.9). These spectra show a clear absorption edge around 192 nm and absorption become insignificant above 400 nm. With an increase in the weight percentage of rGO, the absorbance in the UV-vis spectra increases, and the absorption edge gradually shifts to longer wavelengths. The distinct absorption band of PVA, attributed to the $\pi \rightarrow \pi^*$ electronic transition at 216 nm is evident [35, 36]. Figure. 10 demonstrates that the PVA-rGO nanocomposites exhibit well-defined absorption, with a narrow band at 335 nm, and there is no change in their position as the weight percentage of rGO increases.

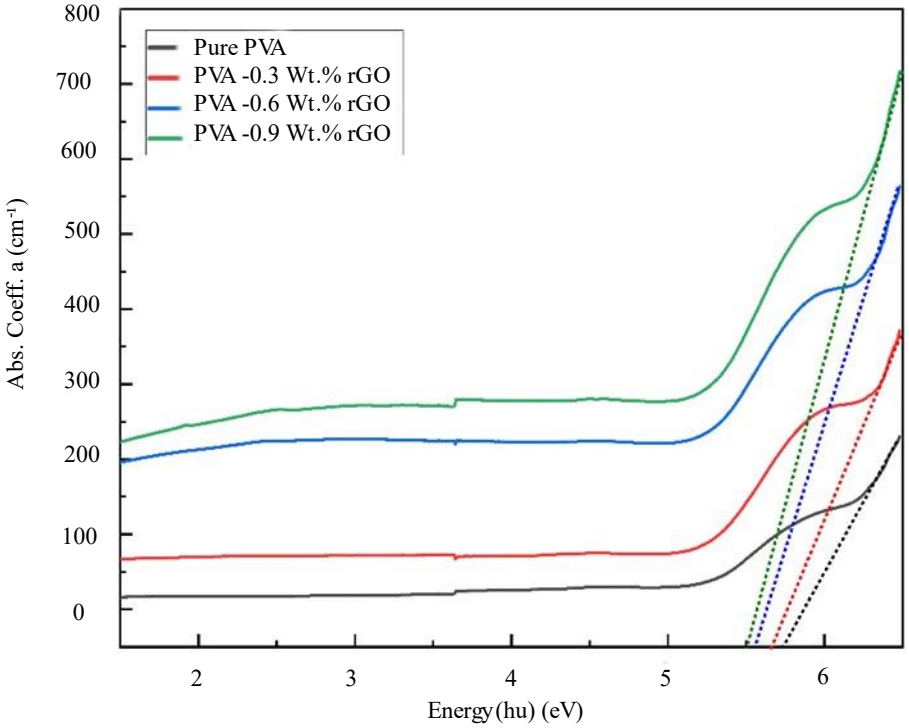

Figure 10. Absorption coefficient vs. energy plots for the PVA-rGO composites.

Direct and indirect bandgap energies

The determination of the optical bandgap of a material is dependent on multiple factors, including but not limited by electromagnetic forces, anisotropy, temperature, and pressure. In order to determine the optical bandgap, Tauc's equation (Equation 4) was used in conjunction with the UV-visible spectrum absorbance data [37].

$$(\alpha h\upsilon)^n = k\,(h\upsilon - E_g) \quad (4)$$

where the parameter k is independent of the energy, E_g indicates the bandgap and 'n' denotes the type of transition. 'n' can take on one of two values: n =1/2 for an indirect allowed band gap transition and n =2 for a direct allowed optical transition. A plot of $(\alpha h\upsilon)^{1/2}$ versus photon energy (E_g) was generated, leading to the determination of the indirect bandgap. This is illustrated in Fig. 11. By extrapolating the linear part of the curve, we draw a line where α=0. The point where the curve intercepts the x-axis is the indirect bandgap of the film samples. The graph shows that as the rGO concentration increased, the E_g values decreased. By incorporating only 0.9 wt% rGO into PVA, the direct band gap was reduced to 5.06 eV (0.9 wt.% rGO) from 6.15 eV for pristine PVA. Previous studies revealed that the band gap of these compounds moves toward lower energies with increasing nanofiller concentration [37]. The direct bandgap was evaluated using the utilisation of the $(\alpha h\upsilon)^2$ *vs*. hν plot, as represented in Fig.12. The direct bandgap was established by extending the linear segment of the plot to $(\alpha h\upsilon)^2=0$. The results showed that by dispersing 0.9 wt.% rGO filler, the direct bandgap energy decreased to 3.86 eV from 4.72 eV. The direct bandgap for PVA is more significant than that for all of the nanocomposites and it decreases with increasing rGO by weight. This indicates that extra energy levels produce localised states in the optical bandgap.

It is also observed that by incorporating only 0.3 wt.% rGO into PVA, the direct and indirect bandgaps are displaced to lower values. The observed decrease in the bandgap energy is a result of the intricate interplay among the polymer matrix and the nanofiller. As a result of these interactions, changes in the electronic structure and crystallinity of PVA were observed. The interaction between rGO and the hydroxyl groups present in the PVA polymer gave rise to the creation of aggregates. This formation had

an impact on the energy levels of PVA [37]. Incorporation of rGO into the polymer matrix produces additional localised defect states in the optical bandgap, which effectively affect the edges of the valence and conduction bands. This phenomenon may be another cause of band gap reduction in composite films.

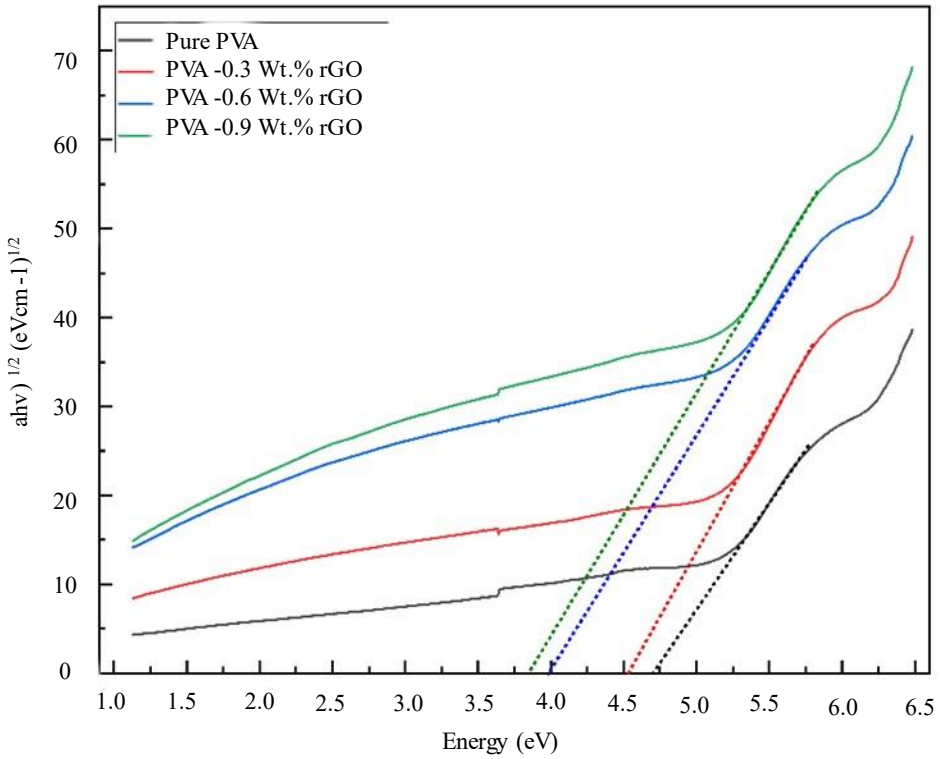

Figure 11. Plot of $(\alpha hv)^{1/2}$ vs hv for PVA-rGO nanocomposite films.

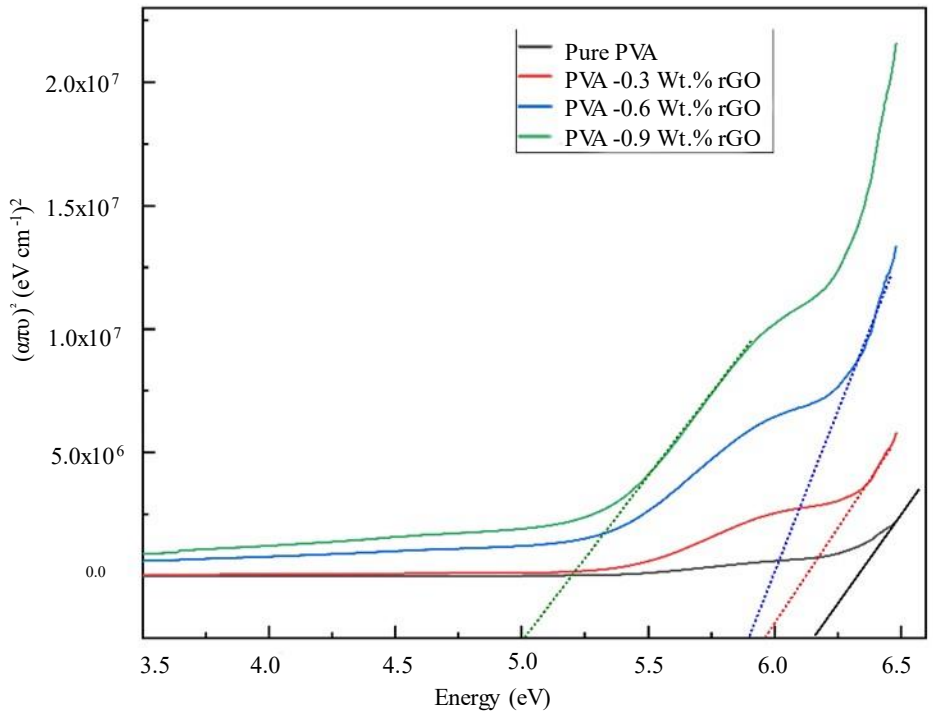

Figure 12. $(\alpha hv)^2$ vs. hv plot for the PVA-rGO nanocomposite films.

Urbach energy and its significance

To check the presence of disorder in the composite films, the Urbach energy E_u was evaluated by plotting the natural logarithm of the absorption coefficient (ln(α)) against the photon energy (hv), as presented in Figure. 13. The determination of the Urbach energy relies on this plot. The observed data show linear behaviour in the vicinity of the fundamental absorption edge, indicating that the PVA-rGO compounds follow the Urbach empirical relation $\alpha = \alpha_o e^{(h\nu/E_u)}$ [38]. As the concentration of rGO increases, the E_u values also increase. Table 3 lists the values of the absorption edge, the direct bandgap (Egd), the indirect bandgap (Egi) and the Urbach energy (E_u) for the PVA-rGO nanocomposites. The Urbach energy reflects the degree of disorder in amorphous semiconductors and is linked to the width of the localised state tails. An increase in Urbach energy suggests a higher presence of confined states in PVA chains [39].

UV shielding studies of PVA-RGO nanocomposites

UV–visible spectroscopy revealed that the PVA polymer absorbs radiation between 200 and 400 nm, revealing that pure PVA can block up to 80.0% of UV radiation. Furthermore, pure PVA has a wide range of bandgap energies, from ~5.06 to 6.15 eV, which is extremely high and corresponds to energies in the UV band (220 to 245 nm). Therefore, PVA films block the passage of UV radiation and protect against UV radiation [40]. Furthermore, the UV absorption of the polymer must be enhanced. Therefore, the UV protection of PVA matrices can be improved by dispersing rGO, resulting in improved UV protection. Figure. 14 shows the wavelength versus percent transmittance curves for various PVA-rGO composite films that cover wavelengths of UV-C (200-280 nm), UV-B (280 nm-320 nm) and UV-A (320 nm-400 nm) wavelengths and in the visible range of electromagnetic radiation. As recommended by UV–visible spectroscopy, the pure PVA film will completely block UV–C radiation [41]. UV-A and UV-B radiation is harmful to human skin and cause skin cancer [41]. Figure. 14 shows that pure PVA has close to zero transmittance up to 215 nm, that is, it completely blocks UV-C radiation. However, above 260 nm, the UV transmission increased to 80.0% at 400 nm. However, a 0.9 wt.% rGO nanofiller by weight significantly reduces the transmittance in the UV range (UV-A and UV-B) from 80.0% to 25.2% and affects the transparency. The high nanophase concentration in these composites increases aggregation within the matrix and reduces the visible transmittance. A sizable extent of UV blocking is noted from 260 to 400 nm with increasing concentrations of rGO.

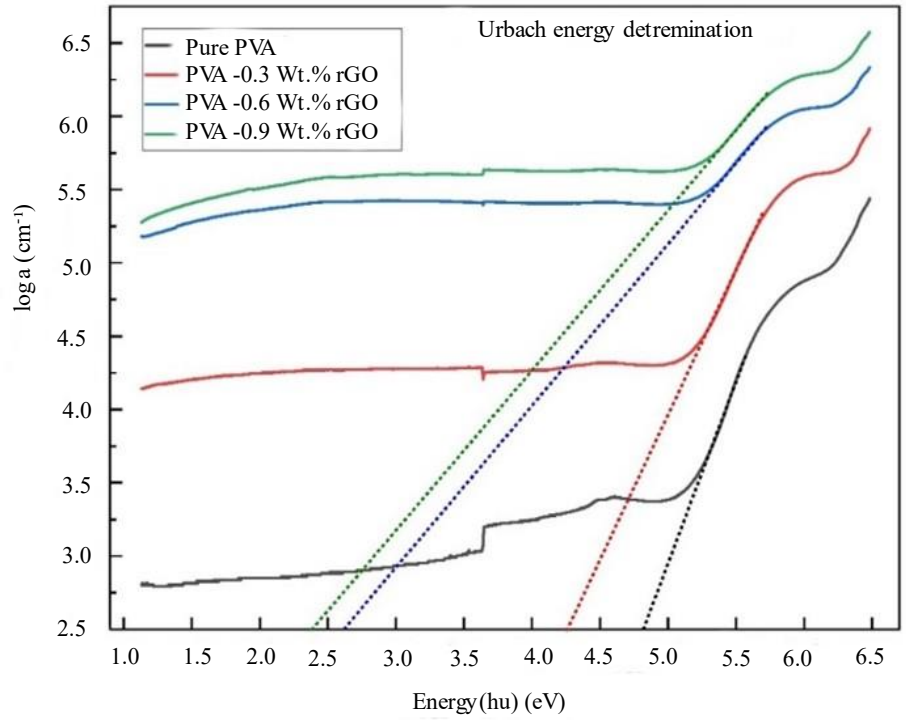

Figure 13. Urbach energy of the PVA-RGO nanocomposites.

Table 3. Absorption edge, direct bandgap, indirect bandgap and Urbach energy values of PVA-rGO nanocomposites.

No.	Composite	Absorption edge (nm)	Direct band gap(E_{gd}) (eV)	Indirect band gap(E_{gi}) (eV)	Urbach energy (E_u) (eV)
1	Pure PVA	216	6.15	4.72	0.402
2	PVA-0.3 wt.% rGO	219	5.97	4.54	0.44
3	PVA-0.6 wt.% rGO	223	5.90	3.98	0.446
4	PVA-0.9 wt% rGO	226	5.0	3.86	0.460

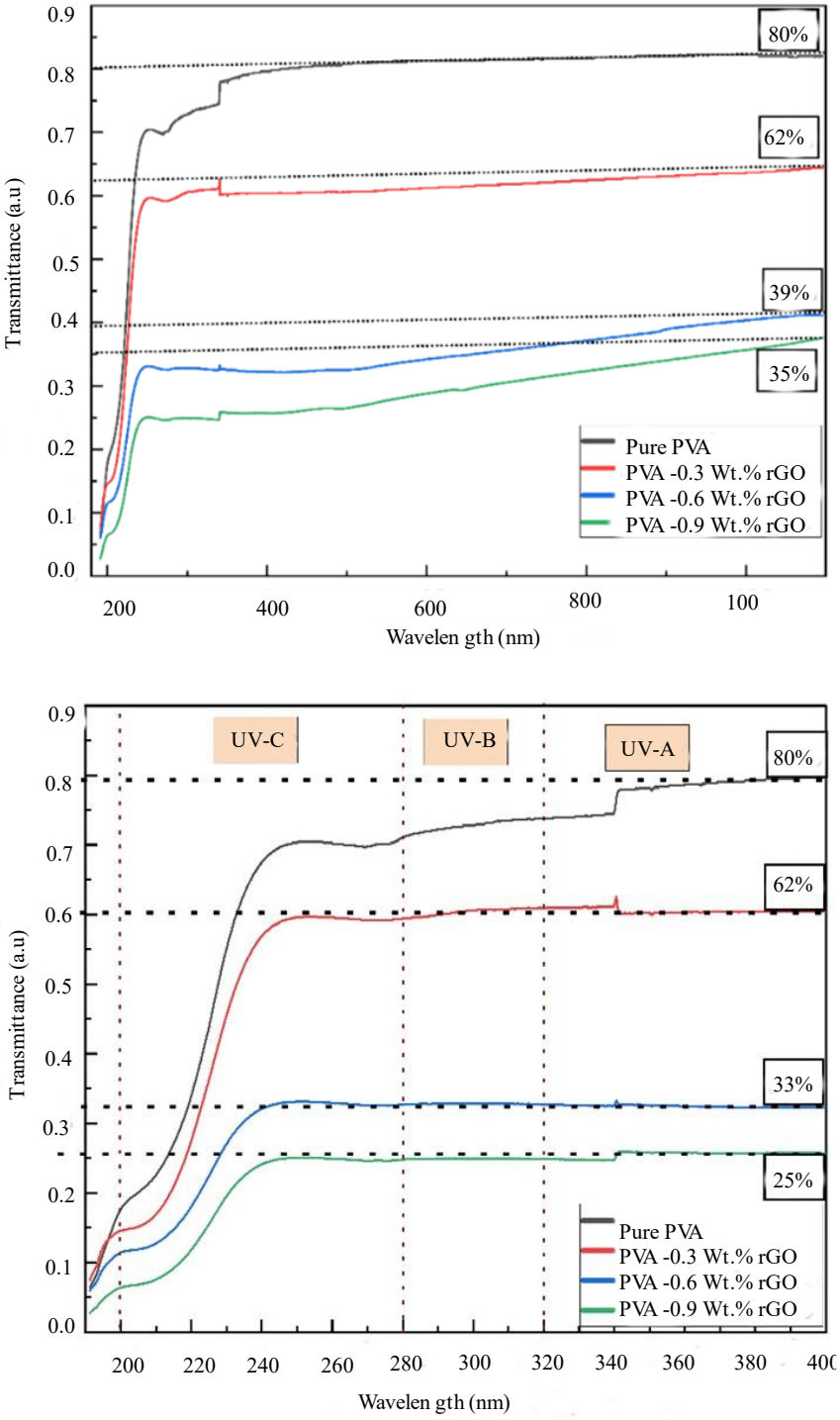

Figure 14. Transmittance vs. wavelength for the PVA-rGO composite films in the UVregion.

An increase in UV blocking is achieved because of the presence of rGO in this range. On the other hand, the visible transmittance decreases with increasing rGO content, and a significant loss of transparency occurs in the composite films. This was attributed to scattering and aggregation at a higher wt.% of the filler [42]. This reduction in transmittance also observed with the help of digital images of the PVA-rGO nanocomposite films with a naked eye, as shown in Figure.2. Therefore, PVA-rGO composite films block UV-A and UV-B radiation more effectively than pure PVA films. The percentage of UV radiation blockage was calculated from transmittance data using equations 5, 6 and 7 in different regions [43].

The percentage of UV-A blocking (320-400 nm) was calculated using Equation 5.

$$\text{UV} - \text{A blocking (\%)} = 100 - \frac{\int_{320}^{400} T(\lambda) d\lambda}{\int_{320}^{400} d\lambda} \text{ (\%)} \quad (5)$$

The percentage of UV-B blocking (280-320 nm) was calculated by Equation 6.

$$\text{UV} - \text{B blocking (\%)} = 100 - \frac{\int_{280}^{320} T(\lambda) d\lambda}{\int_{280}^{320} d\lambda} \text{ (\%)} \quad (6)$$

The percentage of UV-C blocking (200-280 nm) was calculated by Equation 7.

$$\text{UV} - \text{C blocking (\%)} = 100 - \frac{\int_{200}^{280} T(\lambda) d\lambda}{\int_{200}^{280} d\lambda} \text{ (\%)} \quad (7)$$

Table 4 shows detailed UV protection data in the range of 200 to 400 nm for three UV ranges and transparency value of the films. The results confirmed that, compared to those of the PVA films, strong UV-A and UV-B shielding was observed for all the PVA-rGO composites. PVA, with 0.9 wt.% rGO, provides up to 37.7% better UV shielding than PVA and is very impressive. On the other hand, visible light transmission is also necessary in some practical applications, such as protection screens for windows. Therefore, these materials are not suitable for real world applications where transparency is necessary in addition to UV protection. Compared with those of PVA, composites containing 0.6 wt.% reinforcement exhibited a 29.8% improvement in UV shielding. PVA nanocomposite films with 0.6 wt.% rGO nanosheets block ultraviolet wavelengths slightly less than 0.9 wt.%. However, they have more transparency compared to 0.9 wt.% rGO dispersed nanocomposite films. Therefore, the composite films containing 0.6 wt.% rGO are suitable for UV shielding applications wherein transparency also important because of its good visible light transparency value (2.26) and high UV shielding ability (up to 75.4%) (200-400 nm) compared to those of other composites.

The transparency value was calculated using Equation 8 to determine the transparency of the sample.
Transparency value = $\log (T_{600}/d)$ (8)

The transmittance (%) at 600 nm and the thickness of the film are indicated by T_{600} and 'd', respectively [43]. The decrease in transparency of polymer-based composites may be ascribed to factors such as moulding of the polymer, size of the reinforcement nanofiller, aggregation of nanosheets, and light scattering by the particles. Nano and microscopic air pockets are deposited in the matrix during synthesis and cause light to scatter in different directions. Therefore, great care should be taken during the synthesis process to minimise the number of air pockets. Another reason for the scattering could be nanosheet aggregation owing to the large surface area and surface-to-volume ratio of the nanosheets. Aggregates act like larger particles, blocking and scattering light that passes through them, thereby reducing transmission [42]. Therefore, aggregation of rGO is expected to result in strong scattering and loss of transparency. Increased blocking of the UV-A and UV-B radiation ranges may indicate better

dispersion of nanosheets within the matrix at low concentrations. The apparent transparency almost disappears as the concentration increases, that is, at 0.9 wt.% rGO. This is due to the combined effects [41] of a larger particle size; particle agglomeration and decrease in light transmission with increasing rGO wt.%.

Table 4. UV-Shielding Parameters of PVA-rGO Composite Films.

% of UV-blocking					
Sample	**UV**	**UV-A**	**UVB**	**UV-C**	**Transparency value**
PVA	45.6	26.3	29.0	82.1	3.93
PVA-0.3 wt.% rGO	55.5	39.2	40.9	86.5	2.91
PVA-0.6 wt.% rGO	75.4	68.3	68.2	89.9	2.26
PVA-0.9 wt% rGO	83.3	74.9	75.6	99.4	2.15

CONCLUSIONS

The XRD patterns reveal a small decrease in PVA crystallinity because of rGO dispersion at the molecular level within the composites. SEM surface morphology studies showed that the rGO nanosheets were distributed uniformly at lower weights, while agglomeration of the rGO nanosheets was observed at higher weights. However, the distribution of rGO nanosheets is still uniform at higher concentrations. The addition of rGO to the PVA matrix decreased the glass transition temperature. A decrease in T_g and an increase in T_m indicate that the specific heat of the nanocomposite films increased in the amorphous state. The I-V characteristic curves of PVA and composite films deviate from the ohmic nature in the voltage range of ±10 V, i.e., they follow a non-ohmic relationship. DC conductivity (σ_{dc}) increases in a monotonic manner as the rGO content increases. The DC conductivity increases with temperature and nanofiller wt.%. The conductivity increases exponentially in the temperature range 320-380 K, where the polarons have enough energy to hop between many advantageous localised states. The activation energies are more significant at lower temperatures than at higher temperatures. Thus, the interaction between rGO and PVA becomes more pronounced at lower temperatures. UV-visible absorption spectroscopy revealed the characteristic peak of rGO in the spectrum of the PVA-rGO nanocomposites, with a slight blueshift with increasing concentration of rGO. Compared to those of the composite films, the absorption coefficient increases, whereas the direct and indirect bandgaps of PVA decrease as the rGO concentration increases. This demonstrates that localised states are generated in the optical bandgap because of the presence of extra energy levels. Solar cell production, optoelectronics, and other applications involving high frequencies would greatly benefit from using materials with these bandgap values. The findings of this study suggest that the incorporation of rGO nanofiller reinforcement improves UV protection without compromising transparency.

REFERENCES

1. Wang C, Gao H, Liang D, Liu S, Zhang H, Guan H, et al. Effective fabrication of flexible nickel chains/acrylate composite pressure-sensitive adhesives with layered structure for tunable electromagnetic interference shielding. Advanced Composites and Hybrid Materials 2022;5:2906–20. https://doi.org/10.1007/s42114-022-00482-7.
2. Wu Y, Huang K, Weng X, Wang R, Du P, Liu J, et al. PVB coating efficiently improves the high stability of EMI shielding fabric with Cu/Ni. Advanced Composites and Hybrid Materials/Advanced Composites and Hybrid Materials 2022;5:71–82. https://doi.org/10.1007/s42114-021-00401-2.
3. Ashraf M, Wu R, Jhiao W, Chun M, Gorar AAK. Historical progress in electromagnetic interference shielding effectiveness of conventional MG alloys leading to MGLI-based alloys: a review. Advanced Engineering Materials 2023;25. https://doi.org/10.1002/adem.202300732.
4. Zhang Q, Wang Q, Cui J, Zhao S, Zhang G, Gao A, et al. Structural design, and preparation of Ti3C2TxMXene/polymer composites for absorption-dominated electromagnetic interference shielding. Nanoscale Advances 2023;5:3549–74. https://doi.org/10.1039/d3na00130j.

5. Liao Q, Líu H, Chen Z, Zhang Y, Xiong R, Zhou C, et al. Flexible and ultrathin dopamine modified MXene and cellulose nanofiber composite films with alternating multilayer structure for superior electromagnetic interference shielding performance. Frontiers of Physics 2023;18. https://doi.org/10.1007/s11467-022-1234-6.
6. Cheng J, Li C, Xiong Y, Zhang H, Raza H, Ullah S, et al. Recent advances in design strategies and multifunctionality of flexible electromagnetic interference shielding materials. Nano-Micro Letters 2022;14. https://doi.org/10.1007/s40820-022-00823-7.
7. Tan Y, Xue Y, Li K, Liu S, Tan F, Wu X, et al. PVDF/MWCNTs/RGO@Fe3O4/AgNWs composite film with a bilayer structure for high EMI shielding and electrical conductivity. Polymer Composites 2023. https://doi.org/10.1002/pc.27803.
8. Satheesh Goud J, Narsimlu N. Synthesis and Characterization of TiO2 nanoparticles in PVA Polymer Matrix. IOSR Journal of Applied Physics 2021; 13 : 50-55.
9. Ikram M, Inayat T, Haider A, Ul-Hamid A, Haider J, Nabgan W, et al. Graphene Oxide-Doped MGO nanostructures for highly efficient dye degradation and bactericidal action. Nanoscale Research Letters 2021;16. https://doi.org/10.1186/s11671-021-03516-z.
10. Kumar D, Rawat P, Purohit JK. Synthesis MgO nanopowder using Sol-gel technique: A critical review.
11. Khaleel WA, Sadeq SA, Al-Ani I, Ahmed MHM. Magnesium oxide (MgO) thin film as saturable absorber for passively mode locked erbium-doped fiber laser. Optics & Laser Technology/Optics and Laser Technology 2019;115:331–6. https://doi.org/10.1016/j.optlastec.2019.02.042.
12. Hashim A, Abduljalil HM. Structural, optical, and electronic properties of novel (PVA–MGO)/SIC nanocomposites films for humidity sensors. Transactions on Electrical and Electronic Materials/Transactions on Electrical and Electronic Materials 2019;20:218–32. https://doi.org/10.1007/s42341-019-00111-z.
13. Du L, Li Z, Ding S, Chen C, Qu S, Yi W, et al. Synthesis and characterization of carbon-based MgO catalysts for biodiesel production from castor oil. Fuel 2019;258:116122. https://doi.org/10.1016/j.fuel.2019.116122.
14. Qian X, Yin J, Huang J, Yang Y, Guo X, Zhu Z. The preparation and characterization of PVA/Ag2S nanocomposite. Materials Chemistry and Physics 2001;68:95–7. https://doi.org/10.1016/s0254-0584(00)00288-1.
15. Hager MD, Bode S, Weber C, Schubert US. Shape memory polymers: Past, present, and future developments. Progress in Polymer Science 2015;49–50:3–33. https://doi.org/10.1016/j.progpolymsci.2015.04.002.
16. Aslam M, Kalyar MA, Raza ZA. Investigation of structural and thermal properties of distinct nanofillers-doped PVA composite films. Polymer Bulletin 2018;76:73–86. https://doi.org/10.1007/s00289-018-2367-1.
17. Goumri M, Poilâne C, Ruterana P, Doudou BB, Wéry J, Bakour A, et al. Synthesis and characterization of nanocomposites films with graphene oxide and reduced graphene oxide nanosheets. Chinese Journal of Physics/Zhōngguó Wùlǐ Xuékān 2017;55:412–22. https://doi.org/10.1016/j.cjph.2016.12.012.
18. Feng X, Wang X, Xing W, Yu B, Song L, Hu Y. Simultaneous reduction, and surface functionalization of graphene oxide by chitosan and their synergistic reinforcing effects in PVA films. Industrial & Engineering Chemistry Research 2013;52:12906–14. https://doi.org/10.1021/ie402073x.
19. A RR, Srinivas Ch, Narsimlu N. Morphology, and optical absorption studies of RGO reinforced PVB nanocomposite films. Materials Today: Proceedings 2022;67:912–6. https://doi.org/10.1016/j.matpr.2022.07.391.
20. Aslam M, Kalyar MA, Raza ZA. Fabrication of reduced graphene oxide nanosheets doped PVA composite films for tailoring their opto-mechanical properties. Applied Physics A, Materials Science & Processing 2017;123. https://doi.org/10.1007/s00339-017-1035-x.
21. Kadhim MA, Al-Bermany E. Structural and DC-electrical properties of novel PMMA-PVA nanocomposites reinforced with graphene nanosheets. IOP Conference Series Materials Science and Engineering 2021;1067:012120. https://doi.org/10.1088/1757-899x/1067/1/012120.

22. Konios D, Stylianakis MM, Stratakis E, Kymakis E. Dispersion behaviour of graphene oxide and reduced graphene oxide. Journal of Colloid and Interface Science 2014;430:108–12. https://doi.org/10.1016/j.jcis.2014.05.033.
23. Sheik S, Sheik S, Nairy R, Nagaraja GK, Prabhu A, Rekha PD, et al. Study on the morphological and biocompatible properties of chitosan grafted silk fibre reinforced PVA films for tissue engineering applications. International Journal of Biological Macromolecules 2018;116:45–53. https://doi.org/10.1016/j.ijbiomac.2018.05.019.
24. Siwal SS, Zhang Q, Devi N, Thakur VK. Carbon-Based Polymer Nanocomposite for High-Performance Energy Storage applications. Polymers 2020;12:505. https://doi.org/10.3390/polym12030505.
25. Waremra RS, Betaubun P. Analysis of Electrical Properties Using the four-point Probe Method. E3S Web of Conferences 2018;73:13019. https://doi.org/10.1051/e3sconf/20187313019.
26. Ambegaokar V, Halperin BI, Langer JS. Hopping conductivity in disordered systems. Physical Review B, Solid State 1971;4:2612–20. https://doi.org/10.1103/physrevb.4.2612.
27. Patidar D, Jain N, Saxena NS, Sharma K, Sharma TP. Electrical properties of CdS/polyaniline `heterojunction. Brazilian Journal of Physics 2006;36:1210–2. https://doi.org/10.1590/s0103-97332006000700016.
28. Park GT, Chang J. Comparison of properties of PVA nanocomposites containing reduced graphene oxide and functionalized graphene. Polymers 2019;11:450. https://doi.org/10.3390/polym11030450.
29. Sinha S, Chatterjee S, Ghosh J, Meikap AK. Electrical transport properties of polyvinyl alcohol–selenium nanocomposite films at and above room temperature. Journal of Materials Science 2014;50:1632–45. https://doi.org/10.1007/s10853-014-8724-z.
30. Zhang Y, Jiang W. Effective strategies to enhance ultraviolet barrier ability in biodegradable polymer-based films/coatings for fruit and vegetable packaging. Trends in Food Science & Technology 2023;139:104139. https://doi.org/10.1016/j.tifs.2023.104139.
31. Kaur R, Singh KP, Tripathi SK. Electrical, linear, and non-linear optical properties of MoSe2/PVA nanocomposites as charge trapping elements for memory device applications. Journal of Alloys and Compounds 2022;905:164103. https://doi.org/10.1016/j.jallcom.2022.164103.
32. Bouzidi A, Jilani W, Yahia IS, Zahran HY, Assiri MA. Optical Analysis and UV-Blocking Filter of Cadmium Iodide-Doped Polyvinyl Alcohol Polymeric composite films: synthesis and dielectric properties. Journal of Inorganic and Organometallic Polymers and Materials 2020;30:3940–52. https://doi.org/10.1007/s10904-020-01534-5.
33. Tsunekawa S, Fukuda T, Kasuya A. Blue shift in ultraviolet absorption spectra of monodisperse CeO2−x nanoparticles. Journal of Applied Physics 2000;87:1318–21. https://doi.org/10.1063/1.372016.
34. Ali HE, Algarni H, Yahia IS, Khairy Y. Optical absorption and linear/nonlinear parameters of polyvinyl alcohol films doped by fullerene. Chinese Journal of Physics/Zhōngguó Wùlǐ Xuékān 2021;72:270–85. https://doi.org/10.1016/j.cjph.2021.04.022.
35. Muhammad FF, Aziz SB, Hussein SA. Effect of the dopant salt on the optical parameters of PVA:NaNO3 solid polymer electrolyte. Journal of Materials Science Materials in Electronics 2014;26:521–9. https://doi.org/10.1007/s10854-014-2430-0.
36. Aziz SB, Hassan AQ, Mohammed SJ, Karim WO, Kadir MFZ, Tajuddin HA, et al. Structural and optical characteristics of PVA:C-Dot composites: Tuning the absorption of ultraviolet (UV) region. Nanomaterials 2019;9:216. https://doi.org/10.3390/nano9020216.
37. Makuła P, Pacia M, Macyk W. How to correctly determine the band gap energy of modified semiconductor photocatalysts based on UV–VIS spectra. The Journal of Physical Chemistry Letters 2018;9:6814–7. https://doi.org/10.1021/acs.jpclett.8b02892.
38. Gürbulak B, Duman S. Urbach tail and optical characterization of gadolinium-doped TlGaSe2single crystals. Physica Scripta 2008;77:025702. https://doi.org/10.1088/0031-8949/77/02/025702.
39. Hurayra–Lizu KMA, Bari MdW, Gulshan F, Islam MR. GO based PVA nanocomposites: tailoring of optical and structural properties of PVA with low percentage of GO nanofillers. Heliyon 2021;7:e06983. https://doi.org/10.1016/j.heliyon.2021.e06983.

40. Zhao L, Zhang M, Mujumdar AS, Adhikari B, Wang H. Preparation of a novel carbon Dot/Polyvinyl alcohol composite film and its application in food preservation. ACS Applied Materials & Interfaces 2022;14:37528–39. https://doi.org/10.1021/acsami.2c10869.
41. Mohania D, Chandel S, Kumar P, Verma V, Kumar D, Tripathi D, et al. Ultraviolet radiations: Skin Defense-Damage Mechanism. Advances in experimental medicine and biology, 2017, p. 71–87. https://doi.org/10.1007/978-3-319-56017-5_7.
42. Ahmed RM, Soliman TS, Vshivkov SA, Khalid A. Influence of Fe_2O_3@reduced graphene oxide nanocomposite on the structural, morphological, and optical features of the polyvinyl alcohol films for optoelectronic applications. Physica Scripta 2023;98:055928. https://doi.org/10.1088/1402-4896/accb15.
43. Wang YY, Yu H, Yang L, Abdalkarim SYH, Chen W-L. Enhancing the long-term biodegradability and UV-shielding performance of transparent polylactic acid nanocomposite films by adding cellulose nanocrystal-zinc oxide hybrids. International Journal of Biological Macromolecules 2019;141:893-905. https://doi.org/10.1016/j.ijbiomac.2019.09.062.
44. Ye X, Liu R, Qi X-Y, Wang X, Wang Y, Chen Q, et al. Preparation of bioactive gelatin film using semi-refined pectin reclaimed from blueberry juice pomace: Creating an oxidation and light barrier for food packaging. Food Hydrocolloids 2022;129:107673. https://doi.org/10.1016/j.foodhyd.2022.107673.

